

RESEARCH ARTICLE | JUNE 03 2024

Hybrid interfacial cryosoret nano-engineering in photonic resonator interferometric scattering microscopy: Insights from nanoparticles and nano-assemblies

Leyang Liu ; Seemesh Bhaskar ; Brian T. Cunningham  

 Check for updates

Appl. Phys. Lett. 124, 234101 (2024)

<https://doi.org/10.1063/5.0203701>





Instruments for Advanced Science

- Knowledge
- Experience
- Expertise

Click to view our product catalogue

Contact Hiden Analytical for further details:

www.HidenAnalytical.com

info@hiden.co.uk

Gas Analysis



- ▶ dynamic measurement of reaction gas streams
- ▶ catalysis and thermal analysis
- ▶ molecular beam studies
- ▶ dissolved species probes
- ▶ fermentation, environmental and ecological studies

Surface Science



- ▶ UHV-TPD
- ▶ SIMS
- ▶ end point detection in ion beam etch
- ▶ elemental imaging - surface mapping

Plasma Diagnostics



- ▶ plasma source characterization
- ▶ etch and deposition process reaction kinetic studies
- ▶ analysis of neutral and radical species

Vacuum Analysis



- ▶ partial pressure measurement and control of process gases
- ▶ reactive sputter process control
- ▶ vacuum diagnostics
- ▶ vacuum coating process monitoring

Hybrid interfacial cryosoret nano-engineering in photonic resonator interferometric scattering microscopy: Insights from nanoparticles and nano-assemblies

Cite as: Appl. Phys. Lett. **124**, 234101 (2024); doi: 10.1063/5.0203701

Submitted: 15 February 2024 · Accepted: 17 May 2024 ·

Published Online: 3 June 2024



View Online



Export Citation



CrossMark

Leyang Liu,^{1,2}  Seemesh Bhaskar,^{1,2,3}  and Brian T. Cunningham^{1,2,3,4,5,a)} 

AFFILIATIONS

¹Department of Electrical and Computer Engineering, University of Illinois at Urbana-Champaign, Urbana, Illinois 61801, USA

²Nick Holonyak Jr. Micro and Nanotechnology Laboratory, University of Illinois at Urbana-Champaign, Urbana, Illinois 61801, USA

³Carl R. Woese Institute for Genomic Biology, University of Illinois at Urbana-Champaign, Urbana, Illinois 61801, USA

⁴Department of Bioengineering, University of Illinois at Urbana-Champaign, Urbana, Illinois 61801, USA

⁵Cancer Center at Illinois, Urbana, Illinois 61801, USA

^{a)} Author to whom correspondence should be addressed: bcunning@illinois.edu

ABSTRACT

The requirements of augmented signal contrast provided by nanoparticle tags in biosensor microscopy-based point-of-care technologies for cancer and infectious disease diagnostics can be addressed through metallo-dielectric nanoarchitectures that enhance optical scattering and absorption to provide digital resolution detection of single tags with simple instrumentation. Photonic Resonator Interferometric Scattering Microscopy (PRISM) enables label-free visualization of nanometer-scale analytes such as extracellular vesicles and virions, and its applicability can be extended to biomolecular analyte counting through nanoparticle tags. Here, we present template-free, linker-less cryosoret nano-assemblies fabricated via adiabatic cooling (-196°C) as plasmonic nano-antennas that provide high scattering contrast in PRISM. Plasmonic Ag and Au nanomaterials and their cryosorets are evaluated through imaging experiments and simulations based on the finite element method to understand the photo-plasmonic coupling effect at the surface of a photonic crystal (PC) interface. The Ag and Au cryosorets provide at most 8.29-fold and 6.77-fold higher signal contrast compared to their singlet counterpart. Through the simulations, the averaged field magnitude enhancements of 2.77-fold and 3.68-fold are observed for Ag and Au cryosorets when interfacing with PCs compared to bare glass substrates. The hybrid coupling between the localized Mie and delocalized Bragg plasmons of cryosorets and the underlying PC's guided mode resonance provides insights for developing nano-assembly-based nano-tags for biosensing applications.

© 2024 Author(s). All article content, except where otherwise noted, is licensed under a Creative Commons Attribution-NonCommercial-NoDerivs 4.0 International (CC BY-NC-ND) license (<https://creativecommons.org/licenses/by-nc-nd/4.0/>). <https://doi.org/10.1063/5.0203701>

Photonic resonator interferometric scattering microscopy (PRISM) technology has established a strong foothold in optical biosensing by utilizing the interference effect of the scattered light and the reference light in combination with a photonic crystal (PC) substrate.^{1,2} It has emerged as a versatile sensing platform for the label-free imaging of nano-scaled materials with varying physicochemical characteristics. Recently, our laboratory has demonstrated the robust performance of PRISM for real-time identification and quantification of gold nanoparticles (NPs),¹ ferritin protein,² exosomes,² HIV viruses,² and SARS-CoV-2 viruses.³ Among all the studied analytes,

plasmonic NPs have received interest due to their strong scattering signal associated with a near-field enhancement.^{4,5} A wide range of studies have focused on generating field enhancements with different coupling methods, including prism, grating, and waveguide coupling, for various sensing applications.⁶⁻¹¹ In the scope of this paper, we focus on dielectric grating coupling with PCs. When a plasmonic NP is in the vicinity of the PC surface, the PC's inherent guided modes evanescently couple to the hybridized modes of the localized surface plasmon resonance of the NP, generating synergistically augmented surface trapped hotspots. Consequently, the local density of states is

enhanced, leading to strong optical confinement that yields improved far-field signal when illuminated at the combination of wavelength and incident angle that satisfies the on-resonant coupling condition.¹

Fundamentally, yielding a high-contrast signal has been the primary motivation for photo-plasmonics and associated biosensing modalities. In the case of PRISM, this is achieved through two strategies: (1) attenuating the overwhelming background reference light and (2) ameliorating the weak scattered light intensity by interfacial nano-engineering.^{1,12} The first approach usually necessitates additional optics and complex methodologies such as back focal plane engineering,^{13–15} thin-film interference,¹⁶ and polarization filtering.¹⁷ With PCs as imaging substrates, the reference light is automatically attenuated due to its unique spectral response. To pursue the second approach, in the current research, we present the relevance and importance of cryosoret nano-assemblies for boosting the signal contrast vis-à-vis single NP counterparts.^{12,18} Such a nano-engineering approach not only renders a cost-effective and user-friendly route but also provides unprecedented signal contrast. The label-free, linker-less, and template-free cryosoret plasmonic nano-assemblies present compelling candidates for enhanced excitation while interfaced with the PCs, enabling imaging for point-of-care diagnostic applications.^{19–21} By and large, the self-assemblies of nanomaterials are increasingly being explored because of their characteristics that cannot be realized with individual nano-constructs.^{22–26} The delocalized Bragg plasmons (from nanovoids of the cryosoret) and the localized Mie plasmons (from the entire cryosoret) synergistically couple with the guided mode resonance (GMR) of the PCs, enabling high local field enhancement and far-field scattering.^{12,27,28} Although the nanogap antenna effect sustained by the cryosorets in addition to the cavity and void plasmonic hotspots has been earlier utilized for the detection of many biomarkers in spectroscopies, such as surface plasmon-coupled emission (SPCE)^{19,21,29} and surface-enhanced-Raman scattering (SERS),^{20,30} the utility of the three-dimensionally distributed plasmonic hotspots of the cryosorets for contrast enhancement in imaging technologies has not yet been explored. This report aims to accomplish this objective by investigating the judicious ensemble of cryosorets and PRISM through electromagnetic simulations and experimental measurements. The importance of this work is identified in three main aspects: (1) It provides detailed insights into the coupling characteristics between cryosorets and photonic crystals. (2) Combining cryosorets with PRISM technology eliminates the need for expensive imaging components due to its strong signal contrast. (3) This work paves a path for combining cryosorets with molecular biology for biomarker detections, enabling advanced biosensing applications in point-of-care environments.

The PRISM imaging system used in this work has previously been reported [2]. The home-built instrument is based on the concept of interferometric scattering microscopy.^{31,32} Figure 1(a) presents the conceptual schematic of the optical setup of the PRISM system, which uses a 100 mW laser diode operating at 633 nm as the light source. After beam shaping, the illumination light perpendicularly impinges on the PC substrate via Kohler illumination, and approximately 99.5% of the incident light is reflected by the PC (Fig. S1). The weak transmitted light further interferes with the light scattered by the nanometer-scale analyte of interest, forming an interferometric image at the imaging camera. The system is also employed with hardware-based autofocusing to maintain image stability over extended periods.

The PCs are essentially high-contrast dielectric gratings made from depositing a thin layer of TiO₂ (thickness = 95 nm) [the blue layer in Fig. 1(b)] on a patterned glass substrate [the gray layer in Fig. 1(b)]. The PCs exhibit two polarization modes, with a narrower TM mode centered around 617 nm and a wider TE mode centered around 633 nm (Fig. S1). In the scope of this work, we selected the TE mode due to laser wavelength limitation. The PCs are fabricated by a commercial vendor to our design specifications (MOXTEK, Orem, UT) in the form of rectangular pieces (10.2 × 12.7 mm²) and can be purchased from the company. The linear gratings have a period of 380 nm, a depth of 128 nm, and a duty cycle of 65%, as measured by atomic force microscopy and scanning electron microscopy measurements [Figs. 1(c) and 1(d)].

By and large, plasmonic Ag and Au stand out because of their unique optoelectronic properties, ease of bio-functionalization, long-term stability, antimicrobial properties, and anticancer properties, making them interesting tools for therapeutics and diagnostics applications. In this context, we comprehensively investigate the photo-plasmonic coupling efficiency of silver nanoparticles (AgNPs) and gold nanoparticles (AuNPs) as well as their cryosoret nano-assemblies over the PRISM platform. Figure 1(e) presents the synthesis of cryosorets under adiabatic cooling conditions, where the thermal diffusion of homogenous NP solution drives the formation of nano-assemblies. The AgNPs and AuNPs are prepared (using the Turkevich method^{19,21,33}) as a colloidal aqueous solution in a glass vial and subjected to liquid nitrogen (−196 °C) under adiabatic conditions.¹² They are removed at predefined timings to form cryosorets that consist of tunable numbers of particles,¹² thawed to room temperature, and purified via centrifugation and washing (2 times) in Millipore water.

We start the experimental investigation from silver cryosorets (AgCSs) that are formed with 2 (±1), 4 (±2), 6 (±2), 8 (±3), and 10 (±3) AgNPs in line with earlier work.¹² These AgCS samples are labeled from S1 to S10, where the number represents the average number of individual NPs present in the cryosoret. These samples are diluted 1000 times from the stock solution to reach a concentration of approximately 10⁸ particles/ml. Then, 20 μl of the diluted sample is dispensed directly to the PC without any particle immobilization scheme, enabling free movement of the AgCSs over the PC substrate. For each sample, a 10-s video is taken with the PRISM imaging system at a frame rate of a maximum of 290 frames/s, limited by the communication bandwidth. The video is further treated with a moving average filter in the time domain to remove the stationary background and, therefore, enhance the contrast of the AgCSs. The interferometric images of individual AgCSs after video processing are presented in Fig. 2(a), with a full-size exemplary image shown in Fig. S2. The size distribution of the AgCSs is verified via transmission electron microscope (TEM) [Fig. 2(a)]. The recorded videos are treated with the same particle recognition and signal contrast calculation algorithms that are described in detail in our previous reports^{1–3} to identify the signal contrast distribution of each AgCS sample [Fig. 2(b)]. The contrast of the PRISM instrument is expressed as

$$C = 2 \frac{E_{sc}}{E_r} \cos \varphi, \quad (1)$$

where E_{sc} is the scattered electric field magnitude, E_r is the referencing electric field magnitude, and φ is the phase difference between the two fields.^{1,31,32} E_{sc} can be further written as

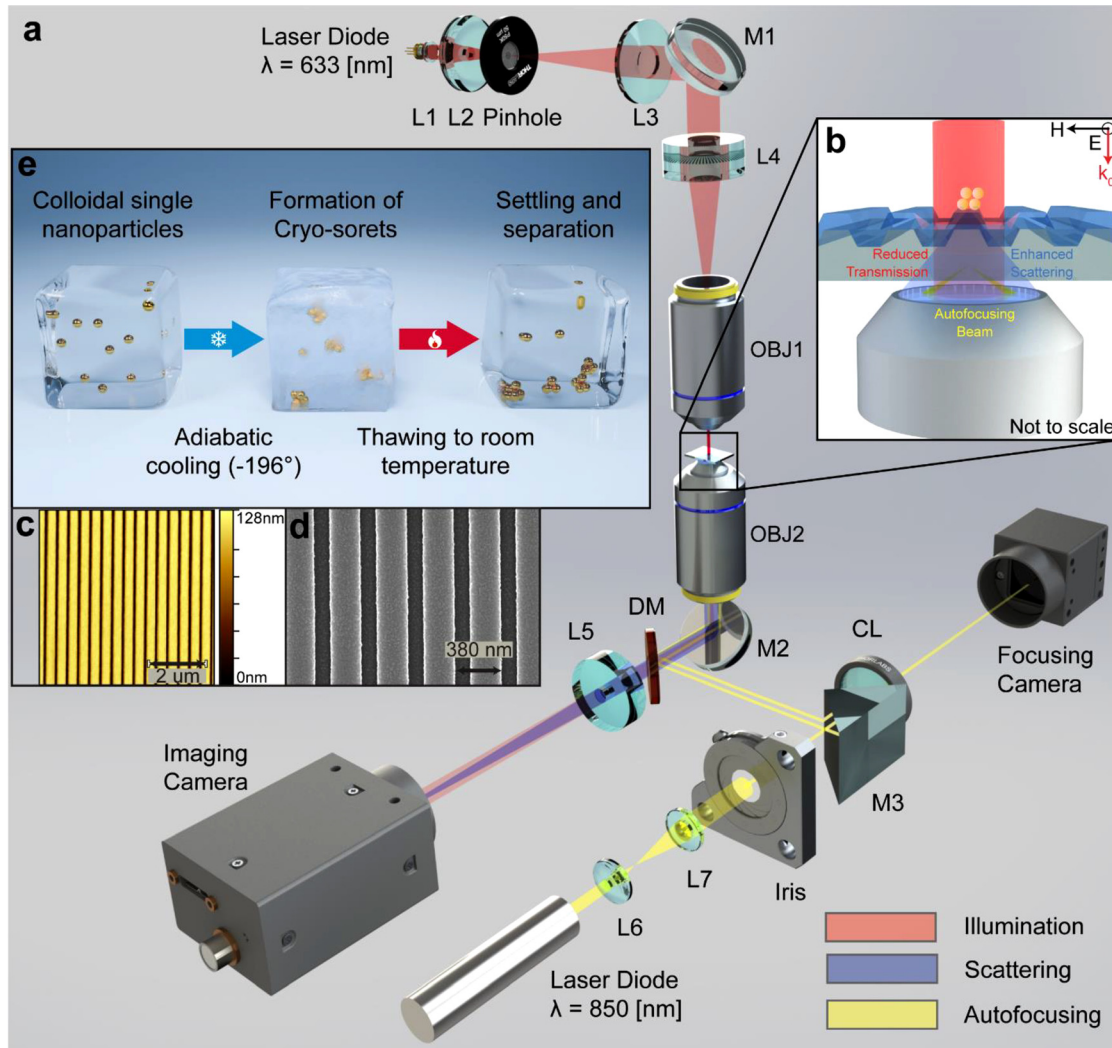


FIG. 1. (a) An illustration of the optical components in the PRISM system. L1–L7: lenses. M1–M3: mirrors. OBJ1–OBJ2: objective lenses. DM: dichroic mirror. CL: cylindrical lens. The red beam denotes illumination light (633 nm). The blue beam denotes scattered light from the sample. The yellow beam denotes autofocusing light (810 nm). (b) A magnified illustration at the sample plane. (c) An illustration showing the formation of cryosets. (d) An AFM image of the PC. (e) An SEM image of the PC.

$$E_{sc} = \alpha E_0, \quad (2)$$

where $\alpha = 3\epsilon_m V(\epsilon_p - \epsilon_m)/(\epsilon_p + \epsilon_m)$ is the complex particle polarizability,³⁴ V is the particle volume, and ϵ_p and ϵ_m are the permittivities of the particle and the embedding medium, respectively. The volume dependence of the scattered field intensity indicates that signal contrast will monotonically and linearly increase as the particle's effective volume increases. We need to point out that, in the context of metallic nanoparticles, LSPR causes a large phase difference between the scattered and reference light, which could be another contrast enhancement mechanism.³⁵ However, in the case of AgCSs and PCs, this trend is undermined by the near-field enhancement of the localized Mie plasmons of the AgCS and the leaky modes of the PC's GMR.² From Fig. 2(b), the signal contrast peaks for the S6 variant, reaching an 8.29-fold magnification compared to single NPs and then

dwindles for the subsequent variants with more NPs per cryoset. Similar phenomena were observed in surface plasmon-coupled fluorescence-based SPCE measurements,^{12,19,29,36,37} where the coupled fluorescence emission increases initially, reaches a maximum for cryoset with the optimum number of NPs (with an adequate balance of hotspots for forward light scattering), and further declines as cryoset size increases. A plausible interpretation for the decrease in signal contrast in the PRISM measurement is the portion of forwardly scattered light increases as the cryoset size increases due to the transition from Rayleigh scattering to Mie scattering. The forwardly scattered light couples to the GMR of the PC and is later outcoupled into the free space, essentially being reflected to the illumination side, especially for cryosets with dimensions approaching the wavelength of the incident light. Therefore, less scattered light is collected by the imaging objective lens underneath the PC substrate, causing a weaker signal

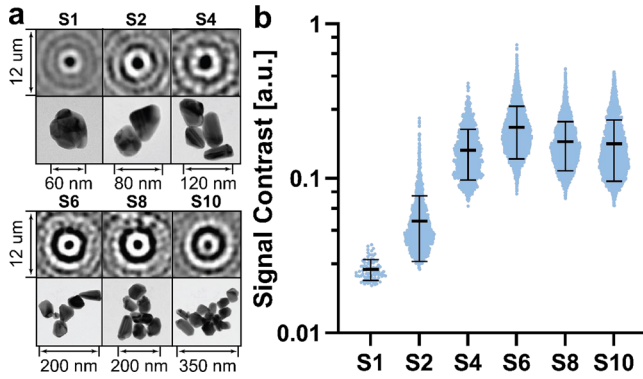


FIG. 2. (a) Selected processed images of different sizes of AgCS obtained with PRISM and their corresponding transmission electron microscope images. (b) The calculated signal contrast of the AgCS samples.

contrast. It is worth noting that the inferences made here are in excellent agreement with the observations made in similar optical outcoupling configurations of the SPCE framework.

In order to draw conclusive insights into the above observations concerning near-field enhancement effects, simulations of the cryosoret-PC hybrid system were performed. The simulations are conducted via the finite element method with the wave optics module of COMSOL Multiphysics. The AgCSs are simulated by bringing together 60 nm-diameter silver spheres with a 0.5 nm gap in between. Their geometries are arranged such that each layer contains four spheres, and at most, three layers exist for the case of S10. The AgCSs are placed directly on the PC top surface or bare glass substrate with a gap of 0.5 nm. Only one period of the PC gratings is modeled, but a periodic condition is applied to the boundaries to model the wave-guiding effect. The geometry for the simulation of each sample is presented in Fig. S3, along with detailed descriptions of the simulation settings. The three-dimensional electric field profile is plotted for each case and is included in Figs. S4 and S5. For consistent comparison, we choose to measure the field intensity at the nanovoid between the first two nanoparticles, and four cross section examples that contain this nanovoid are shown in Fig. 3(a). The cross-sectional field profiles for all cases are included in Figs. S6 and S7. We further calculated the near-field enhancement factor as follows:

$$f = \log_{10} \left| \frac{E}{E_0} \right|, \quad (3)$$

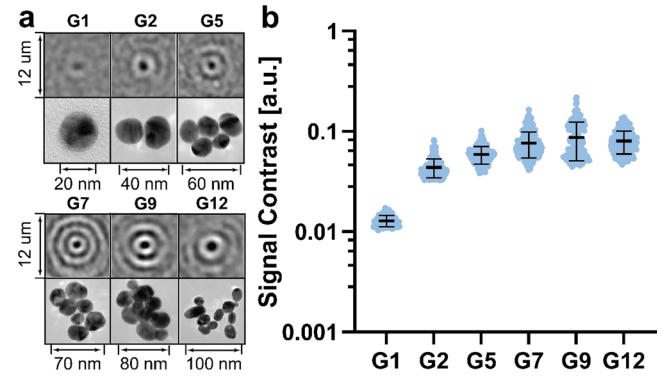


FIG. 4. (a) Selected processed images of different sizes of AuCS obtained with PRISM and their corresponding transmission electron microscope images. (b) The calculated signal contrast of the AuCS samples.

where E is the electric field magnitude and E_0 is the incident electric field magnitude. From the field distribution, it can be observed that for single nanoparticles, the field pattern resembles that of a dipole. For cryosorets, the magnitude of the hotspots occurs at the nanovoids between each nanoparticle. By taking measurements at the same nanovoid across each case, we plotted the hotspot enhancement factor concerning the number of nanoparticles making up the cryosoret [Fig. 3(b)]. The enhancement factor is significantly boosted when AgCS starts to form, as supported by the difference between S1 and S2. However, the field intensity in the nanovoid decreases as the cryosoret grows larger. Other researchers have made the same observation that the hotspot magnitude does not necessarily increase as the nano-assembly gets larger^{23,38–41} due to energy sharing to additional nanovoids; however, the overall integrated enhancement over the entire ensemble of the AgCS does increase as more nanovoids are formed due to collective and coherent plasmonic resonances, supported by increased surface-enhanced Raman spectroscopy signals.^{42–44} By comparing the cases of placing AgCS on PC and glass substrates, one can determine that the near-field enhancement factor of the AgCS on PC model is, on average, 0.443 higher than that of AgCS on glass model. This corresponds to a 2.77-fold near-field electric field magnitude, and the GMR effectuates such enhancement. Under resonance conditions,

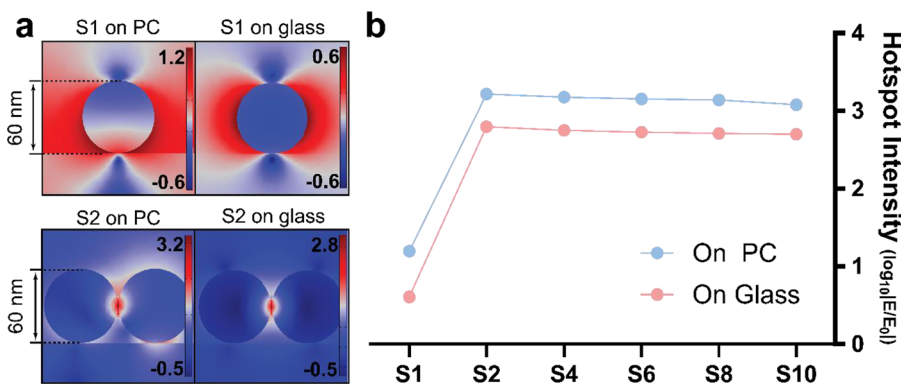


FIG. 3. (a) COMSOL Multiphysics simulations of the near-field electric field enhancement of a single AgNP and an AgCS that is formed by a pair of AgNP on PC and bare glass substrate. (b) The hotspot intensity of each AgCS sample when they are placed on PC and bare glass substrate. For S2–S10, the hotspot is chosen to be in the nanovoid between two adjacent AgNPs.

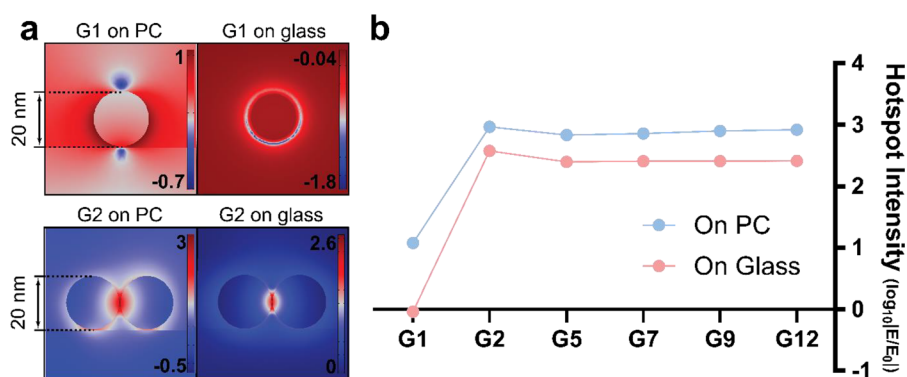


FIG. 5. (a) COMSOL Multiphysics simulations of the near-field electric field enhancement of a single AuNP and an AuCS that is formed by a pair of AuNP on PC and bare glass substrate. (b) The hotspot intensity of each AuCS sample when they are placed on PC and bare glass substrate. For G2–G12, the hotspot is chosen to be in the nanovoid between two adjacent AuNPs.

the evanescent tails of the guided modes reach the peripheral area and augment the field amplitude (Fig. S8). This augmentation is not uniform, causing a location-dependent variable in the enhancement factor. For simulations reported in this Letter, all cryosorets have one of their lower corners centered at the middle of the grating's ridge to ensure they experience the same field amplitude, enabling effective comparisons across all the sample variants.

Similar experimental and simulation analyses are performed on gold cryosorets (AuCSs) to evaluate the photo-plasmonic coupling efficiency. The AuCSs are labeled from G2 to G12, and they are composed of 2 (± 1), 5 (± 2), 7 (± 2), 9 (± 3), and 12 (± 3) single AuNPs. The AuCSs are treated with the same data collection scheme as the AgCSs, and their corresponding processed interferometric images and TEM images are shown in Fig. 4(a). The calculated signal contrast is plotted in Fig. 4(b). Compared to AgCSs, the signal contrast of AuCSs is significantly lower due to their smaller size and higher absorption (engendering Ohmic losses) at the operating wavelength. The same trend is observed in Fig. 4(b), where the signal contrast first peaks at sample G9, reaching a 6.77-fold enhancement compared to singlets, then decreases slightly. We conducted three-dimensional near-field electric field simulations of the AuCSs on PC and glass substrates with the same geometry setup as their silver counterparts. Although the AuCSs on average contains more individual nanoparticles in each sample compared to AgCS, the same geometry setup enables direct comparison of the hotspot magnitude across the gold and silver cases. The three-dimensional and cross-sectional field profiles are included in Figs. S9–S12. The cross section plot of the first two samples for either case is shown in Fig. 5(a), and the field pattern resembles that of the AgCS except for S1 on glass. Due to the absorptive nature of gold at around 600 nm wavelengths, no resonance-induced field enhancement is observed for the case of single AuNPs on a glass substrate. The field enhancement factor at the hotspot between two AuCSs for each sample is plotted to identify the trend [Fig. 5(b)]. The enhancement factor is maximized for the duplex AuCS. However, from G5 to G12, we observed an increased tendency of the field magnitude. On average, the enhancement factor is 0.566 higher for AuCS on PC than on glass substrate, corresponding to a 3.68-fold E field augmentation.

This Letter reported the synergistic combination of cryosorets and PCs with experimental data and simulation results. When interfaced with the PC, cryosorets create strong scattering signals compared to their singlet form, making them valuable labels for tagging and associated biosensing applications. This signal boost becomes extremely important for developing inexpensive, simple, and compact detection

systems for point-of-care diagnostic applications, potentially enabling improved health monitoring in low-resource settings. Cryosoret synthesis is less labor-intensive than traditional template-based and linker-dependent self-assembled nano-assemblies while providing similar or better performance for near-field enhancement. PCs improve the signal contrast by serving as filters for the background light and further strengthen the field intensity through the GMR phenomenon. Results discussed here demonstrate that the field magnitude at the hotspots of the cryosorets is significantly amplified compared to those placed on bare glass substrates. Such precise nano-engineering creates potential pathways for applications encompassing plasmon-enhanced luminescence, Raman spectroscopy, and photocatalysis, thereby presenting valuable insights for advancing the frontiers of the interdisciplinary research portfolio.

See the [supplementary material](#) for information regarding PC spectrum measurements, processed interferometric images, simulation setup parameters, and the three-dimensional field profile of the cryosoret–PC hybrid structure.

The authors thank Joseph Tibbs for his assistance in collecting preliminary data relevant to this work. The AFM, SEM, and TEM measurements were conducted in the Materials Research Laboratory Central Research Facilities, University of Illinois, with the help of the following research scientists: Kathy Walsh, Ying He, and Wacek Swiech. SB acknowledges financial support from Carl R. Woese Institute for Genomic Biology. The authors are grateful for support from NIH (No. R01AI159454).

AUTHOR DECLARATIONS

Conflict of Interest

The authors have no conflicts to disclose.

Author Contributions

Leyang Liu and Seemesh Bhaskar contributed equally to this work.

Leyang Liu: Conceptualization (equal); Data curation (equal); Formal analysis (equal); Investigation (equal); Methodology (equal); Software (equal); Visualization (equal); Writing – original draft (equal). **Seemesh Bhaskar:** Conceptualization (equal); Methodology (equal); Resources (equal); Writing – original draft (equal). **Brian T. Cunningham:** Funding acquisition (equal); Project administration (equal); Supervision (equal); Writing – review & editing (equal).

DATA AVAILABILITY

The data that support the findings of this study are available from the corresponding author upon reasonable request.

REFERENCES

- ¹N. Li, T. D. Canady, Q. Huang, X. Wang, G. A. Fried, and B. T. Cunningham, *Nat. Commun.* **12**(1), 1744 (2021).
- ²L. Liu, J. Tibbs, N. Li, A. Bacon, S. Shepherd, H. Lee, N. Chauhan, U. Demirci, X. Wang, and B. T. Cunningham, *Biosens. Bioelectron.* **228**, 115197 (2023).
- ³N. Li, X. Wang, J. Tibbs, C. Che, A. S. Peinetti, B. Zhao, L. Liu, P. Barya, L. Cooper, L. Rong, X. Wang, Y. Lu, and B. T. Cunningham, *J. Am. Chem. Soc.* **144**(4), 1498–1502 (2022).
- ⁴N. N. Nedyalkov, P. A. Atanasov, and M. Obara, *Nanotechnology* **18**(30), 305703 (2007).
- ⁵P. K. Jain, K. S. Lee, I. H. El-Sayed, and M. A. El-Sayed, *J. Phys. Chem. B* **110**(14), 7238–7248 (2006).
- ⁶I. Abdulhalim, *Nanophotonics* **7**(12), 1891–1916 (2018).
- ⁷S. K. Srivastava, A. Li, S. Li, and I. Abdulhalim, *J. Phys. Chem. C* **120**(50), 28735–28742 (2016).
- ⁸A. Li, S. Isaacs, I. Abdulhalim, and S. Li, *J. Phys. Chem. C* **119**(33), 19382–19389 (2015).
- ⁹M. Abutoama, S. Li, and I. Abdulhalim, *J. Phys. Chem. C* **121**(49), 27612–27623 (2017).
- ¹⁰M. Abutoama, A. Bajaj, D. Li, Y. Wang, L. Jiang, and I. Abdulhalim, *APL Photonics* **5**(7), 076108 (2020).
- ¹¹M. Abutoama and I. Abdulhalim, *IEEE J. Sel. Top. Quantum Electron.* **23**(2), 72–80 (2017).
- ¹²A. Rai, S. Bhaskar, K. M. Ganesh, and S. S. Ramamurthy, *ACS Appl. Nano Mater.* **5**(9), 12245–12264 (2022).
- ¹³M. Liebel, J. T. Hugall, and N. F. van Hulst, *Nano Lett.* **17**(2), 1277–1281 (2017).
- ¹⁴O. Avcı, M. I. Campana, C. Yurdakul, and M. Selim Ünlü, *Optica* **4**(2), 247–254 (2017).
- ¹⁵D. Cole, G. Young, A. Weigel, A. Sebesta, and P. Kukura, *ACS Photonics* **4**(2), 211–216 (2017).
- ¹⁶D. Sevenler, G. G. Daaboul, F. E. Kanik, N. L. Ünlü, and M. S. Ünlü, *ACS Nano* **12**(6), 5880–5887 (2018).
- ¹⁷I.-B. Lee, H.-M. Moon, J.-H. Joo, K.-H. Kim, S.-C. Hong, and M. Cho, *ACS Photonics* **5**(3), 797–804 (2018).
- ¹⁸V. S. K. Cheerala, K. M. Ganesh, S. Bhaskar, S. S. Ramamurthy, and S. C. Neelakantan, *Langmuir* **39**(22), 7939–7957 (2023).
- ¹⁹S. Bhaskar, M. Moronshing, V. Srinivasan, P. K. Badiya, C. Subramaniam, and S. S. Ramamurthy, *ACS Appl. Nano Mater.* **3**(5), 4329–4341 (2020).
- ²⁰M. Moronshing and C. Subramaniam, *ACS Sustainable Chem. Eng.* **6**(7), 9470–9479 (2018).
- ²¹S. Bhaskar, P. Das, M. Moronshing, A. Rai, C. Subramaniam, S. B. N. Bhaktha, and S. S. Ramamurthy, *Nanophotonics* **10**(13), 3417–3431 (2021).
- ²²S. Kadkhodazadeh, J. B. Wagner, V. Joseph, J. Kneipp, H. Kneipp, and K. Kneipp, *Plasmonics* **8**(2), 763–767 (2013).
- ²³P. Pavaskar, J. Theiss, and S. B. Cronin, *Opt. Express* **20**(13), 14656–14662 (2012).
- ²⁴P. Pavaskar and S. B. Cronin, *Appl. Phys. Lett.* **94**(25), 253102 (2009).
- ²⁵K. Li, M. I. Stockman, and D. J. Bergman, *Phys. Rev. Lett.* **91**(22), 227402 (2003).
- ²⁶M. Grzelczak, L. M. Liz-Marzán, and R. Klajn, *Chem. Soc. Rev.* **48**(5), 1342–1361 (2019).
- ²⁷T. A. Kelf, Y. Sugawara, R. M. Cole, J. J. Baumberg, M. E. Abdelsalam, S. Cintra, S. Mahajan, A. E. Russell, and P. N. Bartlett, *Phys. Rev. B* **74**(24), 245415 (2006).
- ²⁸S.-Y. Ding, J. Yi, J.-F. Li, B. Ren, D.-Y. Wu, R. Panneerselvam, and Z.-Q. Tian, *Nat. Rev. Mater.* **1**(6), 16021 (2016).
- ²⁹S. Bhaskar, P. Das, V. Srinivasan, S. B. N. Bhaktha, and S. S. Ramamurthy, *Mater. Res. Bull.* **145**, 111558 (2022).
- ³⁰M. Moronshing, S. Bhaskar, S. Mondal, S. S. Ramamurthy, and C. Subramaniam, *J. Raman Spectrosc.* **50**(6), 826–836 (2019).
- ³¹G. Young and P. Kukura, *Annu. Rev. Phys. Chem.* **70**(1), 301–322 (2019).
- ³²R. W. Taylor and V. Sandoghdar, *Nano Lett.* **19**(8), 4827–4835 (2019).
- ³³M. H. Chowdhury, K. Ray, C. D. Geddes, and J. R. Lakowicz, *Chem. Phys. Lett.* **452**(1), 162–167 (2008).
- ³⁴D. R. H. Craig and F. Bohren, *Absorption Scattering Light by Small Particles* (Wiley, 1998), pp. 82–129.
- ³⁵C.-T. Li, H.-f. Chen, I.-W. Un, H.-C. Lee, and T.-J. Yen, *Opt. Express* **20**(3), 3250–3260 (2012).
- ³⁶A. Rai, S. Bhaskar, K. M. Ganesh, and S. S. Ramamurthy, *Mater. Chem. Phys.* **279**, 125747 (2022).
- ³⁷S. Bhaskar, P. Jha, C. Subramaniam, and S. S. Ramamurthy, *Physica E* **132**, 114764 (2021).
- ³⁸N. M. Abdelazim, M. J. Fong, T. McGrath, C. S. Woodhead, F. Al-Saymari, I. E. Bagci, A. T. Jones, X. Wang, and R. J. Young, *Sci. Rep.* **11**(1), 1528 (2021).
- ³⁹H. D. Trinh, S. Kim, S. Yun, L. T. M. Huynh, and S. Yoon, *ACS Appl. Mater. Interfaces* **16**(1), 1805–1814 (2024).
- ⁴⁰C. Tira, D. Tira, T. Simon, and S. Astilean, *J. Mol. Struct.* **1072**, 137–143 (2014).
- ⁴¹A. K. Sahu and S. Raj, *Gold Bull.* **55**(1), 19–29 (2022).
- ⁴²S. M. Adams, S. Campione, J. D. Caldwell, F. J. Bezares, J. C. Culbertson, F. Capolino, and R. Ragan, *Small* **8**(14), 2239–2249 (2012).
- ⁴³G. Yang, J. Nanda, B. Wang, G. Chen, and D. T. Hallinan, Jr., *ACS Appl. Mater. Interfaces* **9**(15), 13457–13470 (2017).
- ⁴⁴H. Dies, R. Nosrati, J. Raveendran, C. Escobedo, and A. Docoslis, *Colloids Surf., A* **553**, 695–702 (2018).